Earthquake Geotechnical Engineering for Protection and Development of Environment and Constructions – Silvestri & Moraci (Eds)
© 2019 Associazione Geotecnica Italiana, Rome, Italy, ISBN 978-0-367-14328-2

Cyclic lateral loading test and simulation of lateral soil resistance for steel pipe pile with wings

T. Kobayashi & Y. Miyamoto
Department of Architectural Engineering, Division of Global Architecture, Osaka University, Osaka, Japan.

ABSTRACT: Steel pipe piles subjected to lateral loads exhibit toughness even after yielding of the steel, and thus possess a high earthquake resistance. A steel pipe pile with wings attached to its tip can be driven into the ground by rotation. However, it is presumed that the soil around the pile shaft will loosen because the diameter of wings is larger than that of the pile, resulting in reduction of the lateral subgrade reaction of the pile. In this study, cyclic lateral loading tests were conducted to ascertain how the lateral resistance of a pile was affected by wings and simulation analysis was performed by the three-dimensional finite element method.

1 INTRODUCTION

Many different steel pipe piles with flat or spiral-shaped steel wings welded to the pile tip or around the pile (hereinafter, winged piles) have been developed (Inoue 2013) and put into practical use. Compared with cast-in-place concrete piles and bored piles, using these winged piles is one method for reducing the amount of excavated soil and reducing environmental load. Generally, winged piles are installed by applying a rotational torque to the pile shaft to screw the pile into the ground, a method hereinafter referred to as rotational penetration. The diameter of the wing is larger than the outer diameter of the pile. Thus, the extended portion displaces the soil around the pile during construction and can impact ground resistance for the pile.

To date, however, there has been only limited research into the lateral soil resistance around winged piles; these previous studies were conducted by Kuze et al. (2016), Mori et al. (2000), and Nagai et al. (2016). However, as the load tests performed in all previous studies used uniaxial mono-tonic loading, very little research apart from our previous studies (Kobayashi et al. 2013, 2017) has considered lateral soil resistance around the pile due to the cyclic loads expected in an earthquake. An ideal seismic design for winged piles must sufficiently account for lateral resistance of the piles under cyclic loads.

In this paper, we investigate the lateral resistance, bending moment distribution, and sub-grade reaction of the pile with winged pile tips by conducting the cyclic lateral loading tests. And we evaluate the equivalent stiffness and hysteretic damping dependent on the pile displacement using the subgrade reaction-pile displacement relationship, which are required to estimate pile stress during an earthquake. Additionally, the rate of reduction for soil properties is also evaluated in the area through which the wings passed by simulation analysis using the three-dimensional finite element method (3D FEM).

2 IN SITU LATERAL LOAD TESTING

2.1 *Test site*

Tests were performed in the Omitama City, Ibaraki Prefecture, Japan. The N-value distribution and soil boring log for the ground at the test site are shown in Figure 1. Starting from the

ground level, the soil composition of the site ground is kuroboku soil, weathered volcanic ash, volcanic ash and sandy soil. Based on the soil investigation, the surface ground consists of very soft soil.

2.2 *Test piles*

Two test piles were fabricated: one pile with wings (Figure 2) and one pile without wings (Figure 3). The test piles were fabricated using grade STK490 steel with an outer diameter of 267.4 mm and a pipe thickness of 9.3 mm. The pile without wings is referred to as ST, and the pile with wings is referred to as W23 due to the Dw/Dp wing diameter ratio of roughly 2.3, where Dw is the wing's equivalent circular diameter and Dp is the pile's outer diameter. Note here that Dw for the area through which the wing of W23 passes is 606 mm. The wing at the pile tip has a 10° angle of slope and consists of two plates welded onto the tip. A large digging edge fit within the inner diameter of the steel pipe is welded onto the tip of ST. Both test pile tips were closed. The total pile lengths were 5 m. Strain gauges were affixed at 50 points inside the piles in both load directions at 100 mm depth intervals as shown in Figure 4.

2.3 *Loading method*

Figure 4 shows an overview of the test apparatus. The load apparatus comprises a test pile, a reaction force pile, and a hydraulic jack. The test pile and reaction force pile were driven to a depth of GL+200 mm at the pile top by rotational penetration. The piles were loaded by attaching the hydraulic jack in between the reaction force piles and the loading beam joined to the test pile by a high-strength bolt so that the head of the test pile was free to rotate. Load height was set to GL+400 mm. In addition to pile strain, load height displacement of the test pile and reaction force pile were measured with a displacement meter and laser displacement meter, respectively. Note that lateral displacement of the test piles was measured at two points: loading height and GL+100 mm, the latter of which will hereinafter be referred to as reference displacement.

The cyclic loads were displacement-controlled according to the reference displacement. Each load was applied two times each at displacement amplitudes of 1mm, 2mm, 4mm, 6mm, 10mm, 15mm, 20mm, 30mm, 40mm, 60mm, 80mm, 100mm, and 150mm. Subsequently,

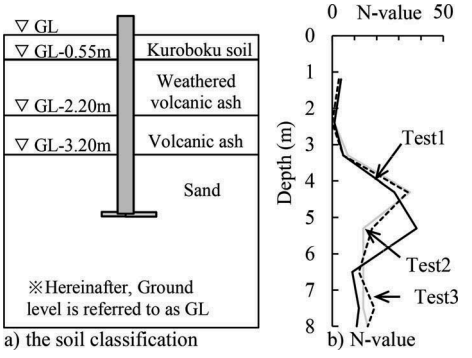

Figure 1. Test results of the soil classification and N-value at the experiment site.

Figure 2. Test pile W23.

Figure 3. Test pile ST.

mono-tonic loading was performed up to +200 mm, and then the test was complete. At peak displacement for the first iteration of each load, the ground was visually inspected for deformation before recording the results.

3 TEST RESULTS

3.1 *Pile head load–reference displacement*

The test results were analyzed at displacement amplitudes of 20 mm, or roughly 10% of pile diameter, and 60 mm, which was the elastic range of the ST pile.

The pile head load-reference displacement relationships until the displacement amplitude of 60 mm are shown in Figure 5. The secant stiffness and hysteretic area of W23 were smaller than those of ST.

3.2 *Ground deformation of ground surface around piles*

Cracks in the ground surface around the test piles are shown in Figure 6. At 20 mm, there was much cracking near the ST pile, whereas a gap had formed between the W23 pile and the surrounding ground with almost no cracking. At 60 mm, both ST and W23 showed increased cracking, with the cracking particularly pronounced in ST compared with W23.

3.3 *Bending moment distribution of piles*

The pile bending moment distributions at displacement amplitudes of 20 mm and 60 mm are given in Figure 7. The maximum bending moment tended to be at deeper location on W23 than on ST.

3.4 *Subgrade reaction–pile displacement relationship around the pile*

Subgrade reaction-pile displacement relationships around the piles at each depth were calculated from the bending moment and curvature distributions as determined using the pile strain

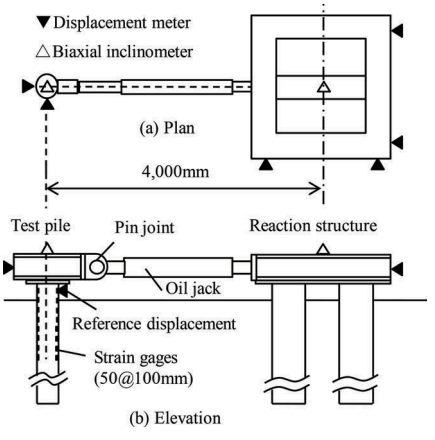

Figure 4. Experimental apparatus and sensor locations.

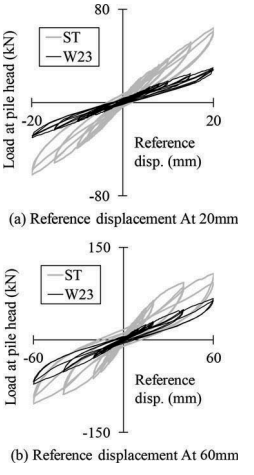

Figure 5. Pile head load–reference displacement relationships.

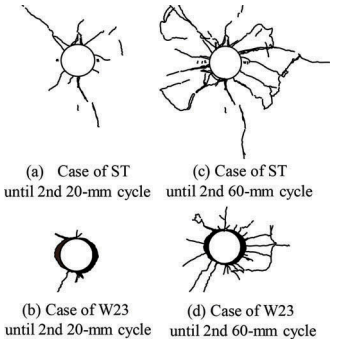

Figure 6. Cracks in the ground surface around the test piles.

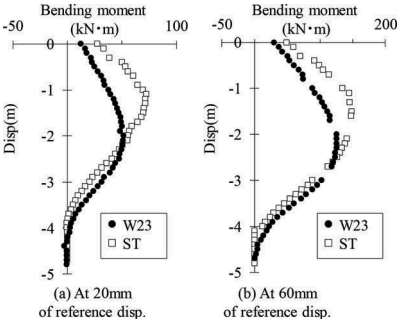

Figure 7. Comparison of the bending moment distributions.

gauges (Kashiwa et al. 2017, 2018). The subgrade reaction distribution was calculated by first approximating the bending moment distribution at an arbitrary pile head displacement with the fifth degree polynomial given by Equation 1.

$$M(z) = a_0 + \sum_{i=1}^{5} a_i z^i \tag{1}$$

where a_0 = M(0) = H $\cdot h_t$; a_1 = H; a_2= 0; M(-4.8) = 0; a_3-a_5 are arbitrary parameters; H is the pile head load; and h_t is the pile projecting length.

The pile curvature distribution at a given pile head displacement was approximated with the fifth degree polynomial given by Equation 2. The curvature at the pile tip here was set to 0. Next, displacement was calculated by taking the second derivative of Equation 2.

$$\phi(z) = b_0 + \sum_{i=1}^{5} b_i z^i \tag{2}$$

where ϕ(-4.8) = 0; and b_0 -b_5 are arbitrary parameters.

The subgrade reaction around pile was obtained by the second-order differentiation of Equation 1. The subgrade reaction-pile displacement relationship at the depths of GL-0.5 m and GL-1.5 m with reference displacements to 20 mm and 60 mm are shown in Figures 8 and 9, respectively. The hysteretic properties of W23 and ST differ according to depth; slip tended to be larger at GL -0.5 m than at GL-1.5 m (see Figure 9(a)).

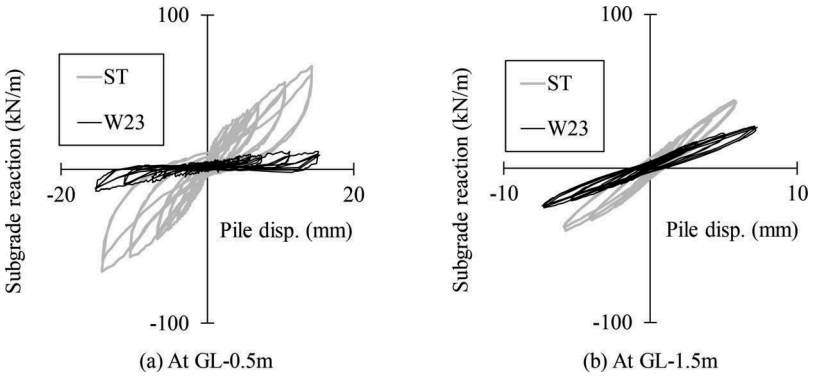

Figure 8. Comparison of subgrade reaction until 2nd-20mm cycle with ST vs W23

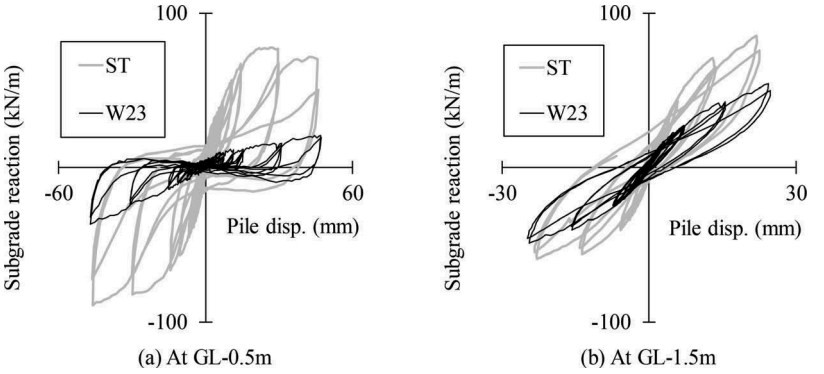

Figure 9. Comparison of subgrade reaction until 2nd-60mm cycle with ST vs W23

4 SECANT STIFFNESS AND HYSTERETIC DAMPING OF SUBGRADE REACTION AROUND THE PILES

4.1 *Analytical method*

The secant stiffness and hysteretic damping calculated from the subgrade reaction-pile displacement relationships of ST and W23 are discussed. The calculation methods for secant stiffness K_{ave} and hysteretic damping h_{eq} are given in Figures 10 and 11, respectively. Where ΔW is absorbed energy by 1 cycle and W is elastic strain energy using secant stiffness.

4.2 *Secant stiffness and hysteretic damping*

The secant stiffness and hysteretic damping are compared by soil classifications. The results for kuroboku soil are given in Figure 12, and those for weathered volcanic ash are given in Figure 13. Secant stiffness decreased with increasing displacement amplitude, regardless of soil classification or presence of wings. Hysteretic damping for ST increased with displacement amplitude but exhibited little differences between soil classifications. Meanwhile, for W23, hysteretic damping tended to be small variant with increasing displacement amplitude in both kuroboku soil and weathered volcanic ash. Minimum ratios of the calculated secant stiffness values for ST and W23, kuroboku stratum is about 0.1 and weathered volcanic ash stratum is about 0.2 roughly.

5 SIMULATION ANALYSIS

Lateral loading test was simulated using LS-DYNA (JSOL Corporation 2007) for the analysis software, a three-dimensional finite element method. The analysis was performed using uniaxial monotonic loading by applying a forced lateral displacement with the pile head free to rotate.

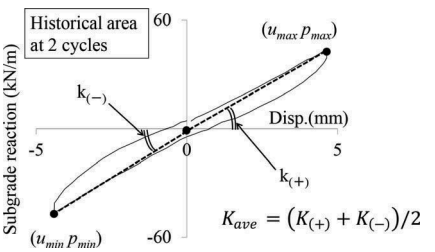

Figure 10. The calculation methods for secant stiffness.

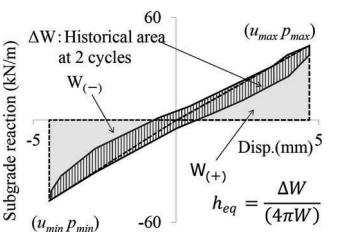

Figure 11. The calculation methods for hysteretic damping.

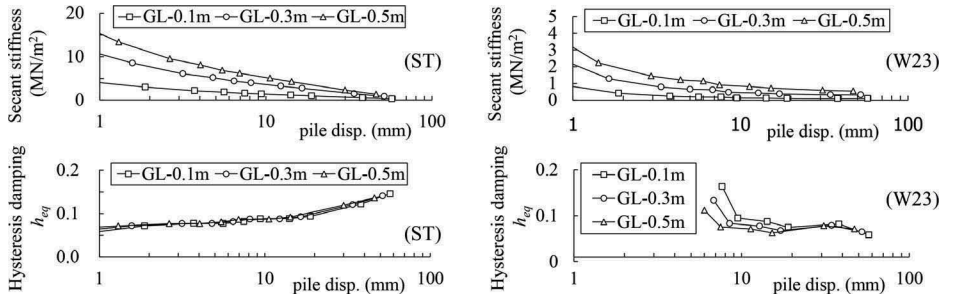

Figure 12. Comparison of secant stiffness and hysteresis damping at kuroboku soil

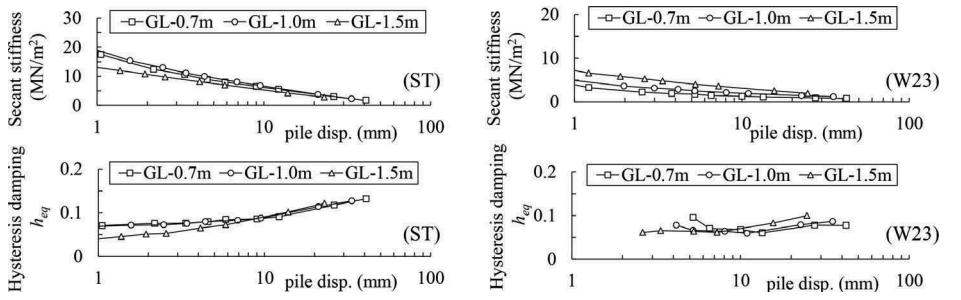

Figure 13. Comparison of secant stiffness and hysteresis damping at weathered volcanic ash

5.1 *Nonlinear soil properties*

The physical properties of the site soil are shown in Table 1, which were obtained by PS logging for all layers and tri-axial compression tests for clay layers from the ground surface to GL-3.2m. The relationships for shear stress-strain behavior of the ground were approximated with the polygonal line of the Hardin-Drnevich (HD) model. The Drucker-Prager yield coefficient was then applied to the shear stress at each soil element to account for dependence on the confining pressure. The HD model is defined as given in Equation 3 (Architectural Institute of Japan 2006):

$$\mathrm{G} = \frac{G_0}{1 + G_0\gamma/\tau_{max}} \tag{3}$$

where G is the shear rigidity; G_0 is the initial shear rigidity; γ is the shear strain; and τ_{max} is the yield shear stress. Both G_0 and τ_{max} were estimated according to soil classification, from the surface layer to GL-3.2 m and from GL-3.2 m down. The calculation method is described below.

5.2 *Kuroboku soil, weathered volcanic ash, and volcanic ash from the surface to GL-3.2 m*

Tri-axial compression tests were used to determine the reference strain $\gamma_{0.5}$ and G_0 at $\gamma = 10^{-4}$. Maximum shear stress τ_{max} of each layer was calculated using Equation 4 below.

$$\tau_{max} = G_0\gamma_{0.5} \tag{4}$$

5.3 *Sandy soil from GL-3.2 m and below*

As tri-axial compression tests were not conducted for these soils, G_0 was calculated using Equation 5 and τ_{max} was calculated with Equation 6, according to the Mohr-Coulomb failure criterion.

Table 1. Material composition of the test site

layer	Depth	Ground classification	Wet density ρ	Cohesion c	Internal friction angle φ	Poisson's ratio ν	Initial shear rigidity G_0	Maximum shear strength τ_{max}	Reduction coefficient of Dw region
	m		t/m^3	N/mm^2	degree		N/mm^2	N/mm^2	
1	-0.55	Kuroboku soil	1.28	0.029	1※	0.292	12.2	0.019	0.1
2	-1.40	Weathered volcanic ash	1.34	0.035	1※	0.333	15.5	0.018	0.2
3	-1.70					0.330	15.5	0.018	
4	-2.20					0.495	15.2	0.018	
5	-3.20	Volcanic ash	1.64	0.090	1※	0.472	15.2	0.024	
6	-4.70	Sand	1.80	0.001	30	0.449	58.3	0.027	1.0
7	-5.70					0.470	35.3	0.038	
8	-7.80					0.496	35.3	0.054	

※ It was set to 1 so as not to diverge due to computational problems.

$$G_0 = \rho V_s^2 \tag{5}$$

$$\tau_{max} = \frac{\sigma_v + \sigma_h}{2} \sin\varphi + c\cos\varphi \tag{6}$$

where ρ is density, V_s is the S-wave velocity from P-S logging, σ_v is the normal stress at the reference depth, σ_h is the lateral stress at reference depth, and φ is the internal angle of shearing resistance.

G_0 and τ_{max} of the disturbed soil around the pile shaft by the wing passage in rotational penetration were reduced using the reduction coefficients in Table1. These coefficients were estimated from the ratios of the calculated secant stiffnesses values of subgrade reactions for ST and W23 described in Section 4.2.

5.4 *Pile-ground modeling*

The pile-ground analysis model used is shown in Figure 14. An elastoplastic solid element was used for the ground. The boundary conditions of FEM model were a fixed base, vertical rollers on the sides, and the soil properties of the ground were divided in-to 8 layers in the depth direction according to soil investigation. Contact conditions between the pile and soil were also set to account for separation and slipping, and re-contact. Thus, the coefficients of friction for clay and sand between the pile and soil were 0.3 and tan30°respectively for the static and dynamic friction coefficients.

The cross section of pile was divided into 16 segments using shell elements. The material properties of the pile have elastic modulus of $E_0 = 2.1 \times 10^5 N/mm^2$ and yield strength of $\sigma_y = 315 N/mm^2$ (mill sheet value). The nonlinear properties were treated as a bi-liner type model, with stiffness being reduced to $1/100E_0$ when yield strength σ_y was exceeded.

5.5 *Simulation results*

The test results and analysis results for the relationship between pile head load and reference displacement are compared in Figure 15. The test and analysis results for ST corresponded well up to the reference displacement of 60 mm, where plasticity of pile presumably begins, whereas the analysis results for W23 exceeded the test results overall. The bending moment distributions at reference displacements of 20 mm are given in Figure 16 for ST and W23. Analysis results for both ST and W23 corresponded well with the test results.

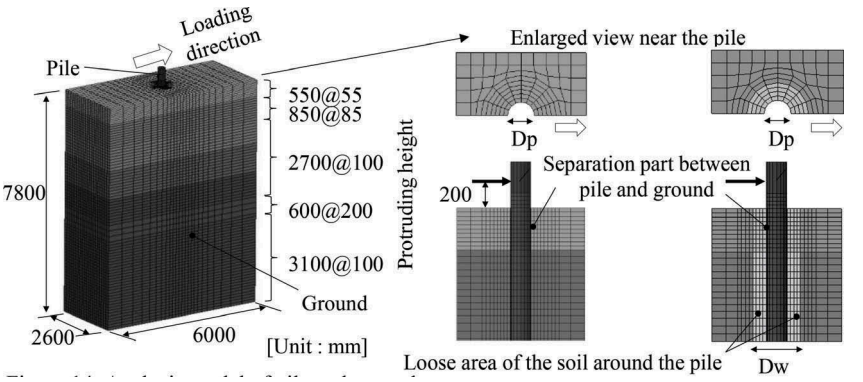

Figure 14. Analysis model of pile and ground.

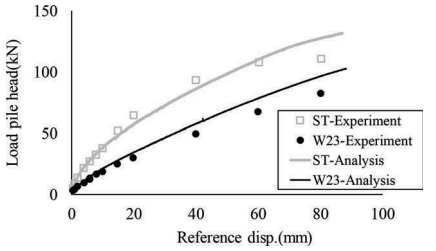

Figure 15. Pile head load-reference displacement relationships.

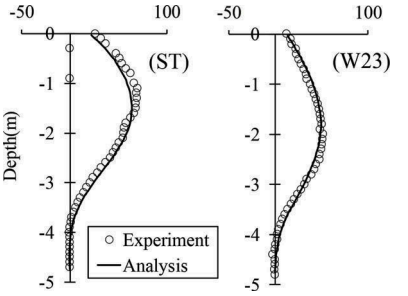

Figure 16. Comparison of the bending moment at 20mm deference disp.

6 CONCLUSIONS

The results obtained from this study are summarized as follows:

1. The lateral stiffness of the winged pile was smaller than that of the pile without wings. Furthermore, at the same displacement, the maximum bending moment of the winged pile was smaller than that of the pile without wings and tended to appear at a deeper depth. The relationships between subgrade reaction and pile displacement around the pile for both piles changed greatly with increasing displacement amplitude.
2. The secant stiffness tended to decrease as the displacement amplitude increases irrespective of the presence or absence of the pile wings. However, the scale of secant stiffness was influenced by the presence or absence of wings and the difference in soil type. The hysteretic damping of the pile without wings tended to increase with increasing displacement amplitude, but the hysteresis damping of the pile wings did not suffer the influence of displacement amplitude and soil type, and it changed with almost constant value.
3. In the 3D-FEM analysis, G_0 and τ_{max} were reduced using reduction coefficient of Dw region in each soil classification, thus showing a good correspondence with the test results for the relationship between pile head load and reference displacement as well as the resulting bending moment distribution.

ACKNOWLEDGMENTS

The authors would like to express their special gratitude to Dr. Eng. Kashiwa and Dr. Eng. Nakano for their useful suggestions for this study and the members of the Miyamoto Lab at

Osaka University, who were of great assistance in compiling this paper. The study was supported by JSPS KAKENHI (Grant No. JP17H03342).

REFERENCES

Architectural Institute of Japan. 2006. *Seismic Response Analysis and Design of Buildings Considering Dynamic Soil-Structure Interaction*. Tokyo: Architectural Institute of Japan.

Inoue, N. 2013. Recent trends in small-diameter steel pipe screw piles. *Foundation Engineering & Equipment (Kisoko)* 41(2): 36–39.

JSOL Corporation. 2007. LS-DYNA Ver. 971 User's Manual Volumes 1, 2.

Kashiwa, H., Kobayashi, T. & Miyamoto, Y. 2017. Modeling method for lateral soil resistance of steel pipe pile with wings in repeated lateral load testing, *Summaries of technical papers of the Japan Association for Earthquake Engineering 2017 meeting*: 2–16.

Kashiwa, H., Kobayashi, T., Miyamoto, Y. 2018. Evaluation of lateral soil resistance for steel pipe pile with wings in repeated lateral load testing. *Summaries of technical papers of the Architectural Institute of Japan annual meeting*: 24(56), 99–104.

Kobayashi, T., Miyamoto, Y., Yamada, H., Furuta, T., Nakano, T., Shimamura, A. & Goto, A. 2017. Research on the lateral resistance of steel pipe pile with wings using lateral load testing, Pt. 1/3. *Summaries of technical papers of the Architectural Institute of Japan annual meeting*: Structural I, 519–524.

Kobayashi, T., Oda, T., Kashiwa, H., Takada, M., Nakano, T. & Miyamoto, Y. 2013. Effects of disturbance around screw pile with wing by penetration on lateral resistance of pile. *Summaries of technical papers of the Architectural Institute of Japan annual meeting*: 551–554.

Kuze, N., Suemasa, N., Inoue, N. & Niki, M. 2016. Property changes of soil around a rotary press-in pile with wings and lateral loading behavior of the pile. *Journal of Structural and Construction Engineering* 81(727): 1455–1465.

Mori, G., Hayashi, M. & Shinohara, T. 2000. Lateral resistance properties of steel pipe screw piles with winged tips. *Proceedings of the 35th Japanese Geotechnical Society Research Presentation*: 1755–1756.

Nagai, H., Tsuchiya, T., Ikeda, A., Sato, Y. & Shimada, M. 2016. Lateral resistance properties of screw piles used with column soil improvement around pile head. *Japanese Geotechnical Journal* 11(2): 127–137.